Chapter 7
Antenna Calibration

David J. Rochblatt

7.1 Introduction

The United States National Aeronautics and Space Administration (NASA) Jet Propulsion Laboratory (JPL) Deep Space Network (DSN) of large, dual reflector, Earth-based antennas is subject to continuing demands for improved performance, performance evaluation, and reliability as a result of escalating requirements for communications, control, and radio science requirements in supporting future missions.

The DSN provides the communications links with many spacecraft of the nation's unmanned space exploration program. In order to satisfactorily perform this mission, each antenna must undergo various calibrations to insure that it is operating as efficiently as possible, and hence delivering maximum information at minimum cost.

As part of the strategy of improving the overall performance capability of the DSN, there has been a steady increase in the operating frequency of these antennas over the years, going from S-band (frequency ~2.3 gigahertz (GHz)), to X-band (frequency ~8.4 GHz), and most recently to Ka-band (frequency ~32 GHz).

One can gain a better appreciation of the implications of these frequency increases for antenna calibration by considering the corresponding wavelengths (λ) of the radiation. Thus, for S-band, λ ~13 centimeters (cm), for X-band λ ~3.6 cm, and for Ka-band λ ~0.9 cm. The essential performance characteristics of an antenna, such as pointing capability and aperture efficiency, are strongly dependent on the wavelength of the radiation being detected. That is why the large (14:1) decrease in wavelength has resulted in the need for much greater

precision of such parameters as reflector surface figure, azimuth track smoothness, and subreflector and beam waveguide (BWG) mirror alignments.

This work describes the development of antenna-calibration instrumentation. The purpose of the antenna calibration instrumentation is to provide reliable tools for the assessment, calibration, and performance improvement of the large number of antenna systems in the DSN. Utilizing the principles of noise temperature measurements, the instrumentation measures and derives the antenna gain, systematic pointing corrections, subreflector focus, as well as the calibration of radio stars[1] used in the assessment of antenna gain. The alignments of the antenna main reflector panels and antenna stability are best measured by coherent holographic techniques (described in Chapter 8 of this book).

As a consequence, a new generation of 34-meter (m) BWG antennas retrofitted with X-band (8.42 GHz) and Ka-band (32 GHz) transmitting and receiving systems is being added to the existing complement of 34-m and 70-m Cassegrain-like antennas (shaped reflectors).

As a result of a systematic analysis of the entire measurement procedure, with particular attention to the noise characteristics of the total-power radiometer (TPR) (Figs. 7-1, 7-2, and 7-3), plus the tropospherically induced radiometer fluctuations and the implementation of new techniques for data acquisition and reduction, it has been possible to obtain measurement precision yielding as much as an order of magnitude improvement over previous methods in the determination of antenna aperture efficiency, and factors of five or more in the determination of pointing errors and antenna beamwidth. This improvement has been achieved by performing continuous, rapid raster scans of both extended and point radio sources. Use of such scans is termed: on-the-fly (OTF) mapping.

The advantages of OTF mapping over the traditional or boresight approach to antenna calibration are that it

1) Removes a major source of error in determining antenna efficiency by eliminating the need for independently derived-source size-correction factors.
2) Takes into account the actual spectrum of the TPR noise fluctuations in determining the optimum integration time during continuous-scan measurements. This includes radiometer flicker noise and tropospheric turbulence effects.
3) Provides a direct comparison of the flux density of one radio source with that of another, thus enabling the accurate calibration of many radio sources for future antenna calibrations.

[1] The term “radio star” refers to any natural, compact source of radiation, which, for example, may actually be a remote galaxy of stars, a region of bright microwave emission in our own Milky Way galaxy, or a planet in our Solar System.

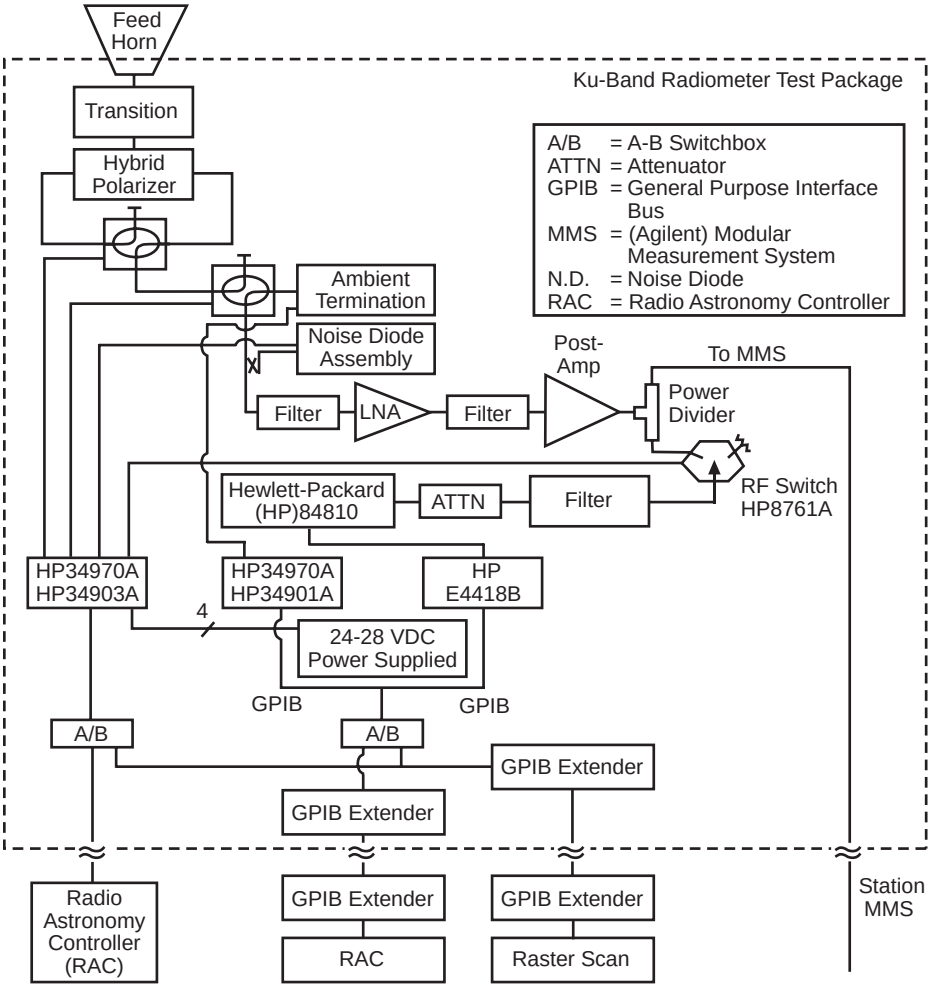

Fig. 7-1. Block diagram of a Ku-band TPR designed for operation with Deep Space Station 13 (DSS-13), 34 m-diameter BWG antenna at 13.8 GHz.

4) Reduces cost and improves the reliability of antenna performance through use of a highly accurate, repeatable, and fully automated system.

While other calibration techniques have advantages for certain applications, OTF mapping accurately provides all of the required calibration data, in the shortest measurement period, including the beam shape as well as the source flux density. The significance of improvements in antenna calibration, performance, or performance evaluation in the DSN can be put in perspective by recognizing that each decibel (dB) of improvement in the quantity gain over noise temperature (G/T) is estimated to be worth about U.S. $160M/dB in terms of mission support capability [1].

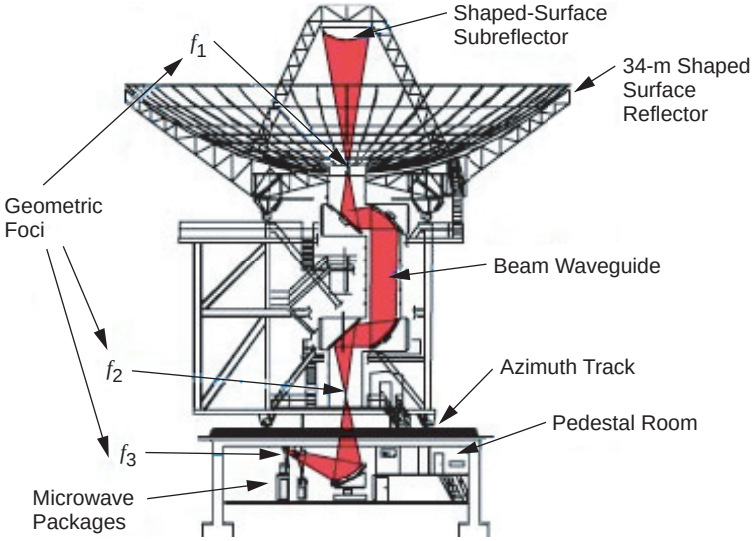

Fig. 7-2. Schematic of a 34-m BWG antenna indicating TPR placement of the microwave packages at *f*3 focus.

Fig. 7-3. 13.8-GHz microwave package TPR during testing prior to installation at DSS-13 at F_3.

In the following section we describe the general requirements for the DSN antenna-calibration effort. This is followed by a discussion of current methods, and their shortcomings, and a final section describes the new approach being now taken in delivering operational Antenna Calibration & Measurement Equipment (ACME) to the DSN.

7.2 Calibration System Requirements

The performance of a DSN antenna must be accurately characterized at the time it comes on line as a new instrument and when new upgrade capabilities are being implemented. Also, certain characteristics must be checked periodically to maintain performance as well as assess the cause of, and correct for, any observed anomaly during normal tracking of a spacecraft.

Calibration procedures require accurate measurement of the various parameters of interest. In the case of antenna calibration, these fall naturally into two categories, those derivable from the measurement of amplitude and phase of a received coherent microwave signal, and those derivable from the measurement of received power from a noncoherent source (such as a radio star). The former case involves the interference of received signals from the antenna under test (AUT) and a small, reference antenna mounted nearby (using the microwave holography described in Chapter 8), while the latter utilizes a total power radiometer (TPR) measuring system to determine the antenna temperature of the source.

The initial calibration consists of precision setting of the individual main reflector panels, precision alignment of the subreflector, determination of aperture efficiency versus antenna elevation angle, and development of a suitable pointing model to permit accurate “blind” antenna pointing.

All of the measurements needed to perform these calibrations involve far-field observations of monochromatic signals transmitted by satellite beacons or broadband radiation from various celestial sources. Holographic measurements are typically performed at X- or Ku-band, based on the availability and elevation angle of suitable geostationary satellite signals, while the remaining measurements utilize in-band S-, X-, and Ka-band frequencies, depending on the equipment planned for the particular antenna under test.

In all cases, some form of sampling of the source radiation is performed as a function of antenna offset from the source. The exact nature of the sampling, as well as the subsequent data processing, determine the precision and accuracy achieved in the overall calibration effort.

In the following section, we briefly enumerate and describe the deficiencies of the conventional approach that has been used in aperture efficiency and pointing measurements. The remainder of the chapter is devoted to a discussion of the approach now being pursued to significantly improve these measurements.

7.3 Conventional Approach to Aperture Efficiency and Pointing Measurements

To measure the gain of large antennas, one can measure the received power from a radio source that has been previously calibrated by independent means [2–5]. A practical method to accomplish this is to measure the received power from the calibration radio source and compare the result with the theoretical result one would measure with a "perfect" antenna. Expressed as a ratio, the result is the aperture efficiency $\eta(\psi)$, where ψ represents the orientation of the antenna, e.g., azimuth and elevation. The formal expression for $\eta(\psi)$ is:

$$\eta(\psi) = \frac{2kT_S(\psi)C_r(\psi)}{AS} \tag{7.3-1}$$

where

A = antenna aperture physical area, m^2

C_r = source size correction factor, unitless measure

k = Boltzmann's constant (1.38065×10^{-23} W/K-Hz)

S = flux density of radio source, W/(m^2-Hz)

T = temperature, kelvin (K)

T_S = antenna noise temperature increase due to the source, kelvin (K)

The antenna aperture, A, for a circular dish of diameter d is the geometrical area $A = \pi d^2/4$. In Eq. (7.3-1), it is assumed that the antenna points perfectly. In practice we attribute the losses due to mispointing of the antenna separately.

While radio astronomy telescopes are designed for maximum beam efficiency, the DSN antennas are designed for maximum aperture efficiency. Beam and aperture efficiencies are functions of the aperture illumination function. The aperture efficiency is at maximum with no taper, while the beam efficiency is at maximum with full taper. The aperture efficiency $\eta(\psi)$ is affected by the areas of the noise shield, subreflector, and struts blockages; the strut shadow; the amplitude taper illumination; the reflector surfaces root mean square (rms) errors; and the ohmic losses.

In radio astronomy, the process of measuring the antenna aperture efficiency is further complicated by the fact that sources for which radio-frequency (RF) flux densities have been accurately measured tend to be rather large in angular size relative to the antenna pattern of a large-aperture radio telescope such as a DSN antenna. In practice, the small angular width of the antenna beam partially resolves the angular structure of the radio source with the result that some of the radio flux density is not collected by the antenna when it is pointed "on source." A "correction for source size" $C_r(\psi)$, is

typically used to compensate for this effect. Note that the value of C_r is expected to vary with antenna orientation ψ because both the beam shape and the angular orientation of the radio source change as the source rises and sets across the sky.

Each of the quantities, C_r and S, contains a source of error, and the measurement method used to determine each must be addressed in any search for improvement. Note that in the DSN we define T at the input to the feedhorn aperture; and therefore, the antenna aperture efficiency, η, is also defined at the same reference point.

7.3.1 Source Size Correction Factor

The source size-correction factor is designed to account for the flux density of an extended source not collected by the antenna, and it is best understood with reference to the fundamental radiometric equation from which Eq. (7.3-1) is derived,

$$kT_S\left(\psi;\theta,\phi\right) = \tfrac{1}{2}\eta_\upsilon\left(\psi\right)A\iint_{\text{source}} B_\upsilon\left(\theta',\phi'\right)P_{n,\upsilon}\left(\psi;\theta'-\theta,\phi'-\phi\right)d\Omega' \qquad (7.3\text{-}2)$$

where

B_υ is the source brightness function,

$P_{n,\upsilon}$ is the normalized antenna power pattern, and

(θ,ϕ) are rectangular, angular coordinates relative to the source center [6,7].

Here, we have been specific regarding the dependence of various quantities on the antenna pointing direction, ψ, and the operating frequency, υ, as well as the fact that the measured system noise temperature increase due to the source, T_S, depends on the antenna pointing.

The integral appearing in Eq. (7.3-2) is the source flux density collected by the antenna, and is smaller than the total source flux density emitted by the source

$$S_\upsilon = \iint_{\text{source}} B_\upsilon\left(\theta,\phi\right)d\Omega \qquad (7.3\text{-}3)$$

unless the source is much smaller in extent than the antenna main beam and the antenna is accurately pointed at the source. Equation (7.3-2) may be cast into the form of Eq. (7.3-1) by defining the source size correction factor,

$$C_{r,\upsilon}(\psi,\theta_m,\phi_m) = \frac{S_\upsilon}{S_{\text{coll},\upsilon}(\psi,\theta_m,\phi_m)} \geq 1 \tag{7.3-4}$$

where

$$\begin{aligned} S_{\text{coll},\upsilon}(\psi)\big|_{\max} &= S_{\text{coll},\upsilon}(\psi,\theta_m,\phi_m) \\ &= \iint_{\text{source}} B_\upsilon(\theta',\phi') P_{n,\upsilon}(\psi;\theta'-\theta_m,\phi'-\phi_m)\, d\Omega' \end{aligned} \tag{7.3-5}$$

is the *maximum* flux density collected by the antenna, that is, the antenna noise temperature field, $T_\upsilon(\psi;\theta,\phi)$, must be explored at a given elevation angle until the maximum value corresponding to the coordinates $(\theta_m,\phi_m)$is found. It should be noted that these coordinates will not be those for the source center unless the source happens to be symmetric.

Equations (7.3-4) and (7.3-5) imply that the determination of $C_{r,\upsilon}(\psi)$ requires a knowledge of the source brightness function and the normalized antenna power pattern. For those circumstances where $C_{r,\upsilon}(\psi)$ is within a few percent of 1, the usual approach to its evaluation has been to estimate both of these functions by symmetric Gaussians, in which case one obtains the oft-quoted formula

$$C_{r,\upsilon} = 1 + \left(\frac{\Theta_S}{\Theta_B}\right)^2 \tag{7.3-6}$$

where Θ_S and Θ_B are the source and antenna beam widths, respectively. For a disk-like distribution, the correction factor is

$$C_{r,\upsilon} = \left[\frac{1-e^{-x^2}}{x^2}\right]^{-1} \tag{7.3-7}$$

where,

$$x = (4\ln 2)^{\frac{1}{2}} * R/\Theta_B, \tag{7.3-8}$$

and R is the angular radius of the disk [8].

However, many commonly used sources have corrections approaching 100 percent for a large antenna operated at high frequency. The source size-correction value for Virgo A, at Ka-band, on the 70-m antenna, for example, is

calculated to be 1.90. At S-band, the value for source size correction for same source on the 70-m antenna is 1.205 [7]. Under these circumstances, the computation of the source-size correction must be carried out with more realistic functional representations of the source structure, and the source of these has been brightness maps measured with very long baseline interferometry (VLBI) arrays, or large antennas such as the 100-m antenna at Bonn, Germany.

It is possible, in principle, to perform a proper deconvolution of such maps to compute Eq. (7.3-5). Thus, an average brightness map obtained with an antenna having an equivalent normalized far-field power pattern, $P_{0,n}(\theta,\phi)$, given by

$$B_0(\theta,\phi) = \frac{1}{\Omega_0}\iint_{\text{source}} B(\theta',\phi') P_{0n}(\theta-\theta',\phi-\phi')\, d\Omega' \tag{7.3-9}$$

where Ω is the equivalent measuring beam solid angle, where we now drop the explicit frequency and elevation angle notation, and where for simplicity we assume beam symmetry so that the integral has the form of a convolution. Then, taking the Fourier transform of Eqs. (7.3-5) and (7.3-9), we have

$$\begin{aligned} \tilde{S}(\mu,\nu) &= \tilde{B}(\mu,\nu)\tilde{P}_n(\mu,\nu) \\ \tilde{B}_0(\mu,\nu) &= \frac{1}{\Omega_0}\tilde{B}(\mu,\nu)\tilde{P}_{0n}(\mu,\nu) \end{aligned} \tag{7.3-10}$$

from which we obtain

$$\tilde{S}(\mu,\nu) = \Omega_0 \frac{\tilde{P}_n(\mu,\nu)}{\tilde{P}_{0n}(\mu,\nu)} \tilde{B}_0(\mu,\nu) \tag{7.3-11}$$

so that performing the inverse Fourier transform yields $S_{\text{coll}}(\theta,\phi)$ from which $S_{\text{coll}}(\theta_m,\phi_m)$ may be found. In the above, (μ,ν) are the spatial frequency coordinates. This procedure has in fact been used to generate the C_r values currently used in the DSN for calibration purposes [7,8], but the approach has a number of limitations that become serious at high frequencies:

1) Maps are usually not available at the frequency of interest so that an interpolation procedure must be used to estimate a map at the required frequency.
2) Large antennas have significant flexure as a function of elevation angle due to gravitational loading resulting in aberrations that affect the beam pattern,

so that the values of C_r ought to be calculated as a function of elevation angle (see Eq. 7.3-4)).

3) Information on the mapping beam solid angle and shape is often approximate or unavailable in the literature. This can be obtained from holographic measurements [13].

An alternative approach is thus called for that eliminates the need for source size corrections, and this approach is described in a following section.

7.3.2 Flux Density

Since source flux densities are determined from the same equation used to determine aperture efficiency, Eq. (7.3-1), all of the sources of error attendant the latter must apply to the former as well. Thus, while the very brightest sources can be measured with a low-gain system such as a horn, for which calibration is relatively straightforward, the transfer of information from strong to weak sources, which are compact enough to serve as reasonable calibrators for large antennas, must be carried out with larger antennas. Then, Eq. (7.3-1) leads to the result

$$\frac{S_1}{S_2} = \frac{T_1}{T_2}\frac{C_{r_1}}{C_{r_2}} \tag{7.3-12}$$

where the subscripts refer to measurements of two different sources with the same antenna, and we see that not only antenna temperatures, but also source-size corrections, enter into the calculation of flux density ratios for different sources.

A survey of the literature on flux density measurements shows that the use of inaccurate C_r values contributes significantly to the error budget for such measurements [3,5,7,8], so that eliminating the need for such a correction would result in a significant increase in the accuracy of flux density determinations.

7.3.3 Source Temperature

The basic method for measuring the system noise-temperature increase due to a source involves some form of on-source, off-source subtraction. In the conventional approach (sometimes termed “autobore”) this is accomplished by a boresight technique in which the antenna is successively offset in a given direction, say θ, relative to the source, by ±5, ±1/2, and zero antenna half-power beamwidths (HPBW). The resulting five data points are then fitted to a Gaussian function plus a linear background to account for the decrease in system noise temperature with elevation angle; and from this fit, the maximum,

or peak source noise temperature, and θ pointing error and beamwidth are determined. This pointing error is then used to execute an orthogonal boresight in the ϕ direction, and the process is repeated as the source is tracked.

While this works well at S-band, it is less satisfactory at X-band, and unsatisfactory at Ka-band, especially with regard to the pointing determination, where (for example) it has been unable to provide the requisite precision to meet the radio science requirements for the Cassini mission to Saturn [9]. Additionally, the method is inherently slow since each of the five measurements in a given direction requires that the antenna servos and mechanical structure settle at the offset specified before a noise-temperature measurement is made. A further problem is that the Gaussian fitting function only approximates the actual profile of the noise temperature measurement (which follows the antenna far-field pattern function), and for an extended source this approximation may not be very good.

In view of these limitations, one would like to have a source noise-temperature measurement of inherently greater accuracy. This would not only improve our knowledge of antenna gain and pointing, but it would also improve the calibration of weak sources by the comparison method described above.

In the following section we describe a new approach to the calibration of large, ground-based antennas that significantly improves the precision achieved by reducing or eliminating the above-noted sources of error inherent with present methods.

7.4 The Raster-Scan Method

The key to reducing the error sources discussed in the previous section lies in making system noise temperature measurements over a finite area of sky including the source, rather than along orthogonal cuts through the temperature profile. Thus, integration of Eq. (7.3-2) over the two dimensional angular field (θ, ϕ) gives

$$k \iint_{\substack{\text{source} \\ +\text{beam}}} T_S(\theta, \phi)\, d\Omega = \tfrac{1}{2} \eta A \Omega S \qquad (7.4\text{-}1)$$

where Ω is the antenna beam solid angle, and we have dropped the explicit frequency and elevation angle notation for simplicity.

If we now consider the application of the above equation to two sources, the equivalent of Eq. (7.3-12) becomes

$$\frac{\iint_{\substack{\text{source}\\+\text{beam}}} T_1(\theta,\phi)\,d\Omega}{\iint_{\substack{\text{source}\\+\text{beam}}} T_2(\theta,\phi)\,d\Omega} = \frac{S_1}{S_2} \tag{7.4-2}$$

as a result independent of source size corrections.

If the source considered in Eq. (7.4-1) is small enough relative to the main beam to be considered a point, then its brightness may be represented by

$$B(\theta,\phi) = S_p\,\delta(\theta)\,\delta(\phi) \tag{7.4-3}$$

where $\delta(x)$ is the Dirac delta function and S_p is the flux density of a point source. Then, Eqs. (7.3-4) and (7.3-5) show that C_r = 1 so that Eq. (7.3-1) becomes

$$\eta = \frac{2kT_p}{AS_p} \tag{7.4-4}$$

If the flux density, S_p, of this point source is known, then Eq. (7.4-4) immediately yields the aperture efficiency in terms of the peak source temperature. However, it is frequently the case that point sources bright enough for calibration purposes are also variable, so that one may not have a-priori knowledge of S_p. In this case, Eq. (7.4-2) may be used to determine S_p by comparison with an extended, calibrated source whose flux density, S_c, is known. Then, by combining Eqs. (7.4-2) and (7.4-4), we have

$$\eta = \frac{2kT_p}{AS_c}\,\frac{\iint T_c(\theta,\phi)\,d\Omega}{\iint T_p(\theta,\phi)\,d\Omega} \tag{7.4-5}$$

which now becomes the fundamental equation for determining aperture efficiency. These equations can now be arranged to solve for the source size corrections as follows:

$$C_r(\psi,\theta_m,\phi_m) = \frac{S_c}{S_p} = \frac{T_p(\theta_m,\phi_m)\iint T_c(\psi,\theta,\phi)d\Omega}{T_c(\theta_m,\phi_m)\iint T_p(\psi,\theta,\phi)d\Omega} \tag{7.4-6}$$

The data for the computation implied by Eqs. (7.4-5) and (7.4-6) are the temperature fields $T_p(\theta,\phi)$ and $T_c(\theta,\phi)$ for the point and extended calibration source, respectively; and these are obtained by scanning the antenna beam across the source in a raster pattern, similar to a (non-interlaced) television (TV) scan (Fig. 7-4). In Fig. 7-4, the raster-scan is designed to image the planet at the center of the image. The deviation of the image position from the center is the result of pointing errors introduced by the antenna combined with difficult refraction correction computations at the low elevation angle of 7.6 deg. The color dots above and below the scans are the computed observation coordinate of the source at the mid point of each scan. The combined data from the 33 scans are then displayed at the top left of the display.

All the terms on the right side of Eq. (7.4-5) are either known values, or they are measured by the OTF-mapping system.

It should be noted here that the ratio of the integrals appearing in Eqs. (7.4-5) and (7.4-6) is, by Eq. (7.4-2), just the ratio of the flux densities for the two sources, that is, a constant. Thus, the measurement strategy should involve the alternate scanning of the two sources over a small but finite elevation change so that the data points corresponding to each integral, as a function of elevation, can be fitted to a linear function, or perhaps quadratic function. Then, it should be found that the ratio of these two fitting functions is constant and equal to S_c / S_p. These results illustrate some of the valuable features of the OTF-mapping system:

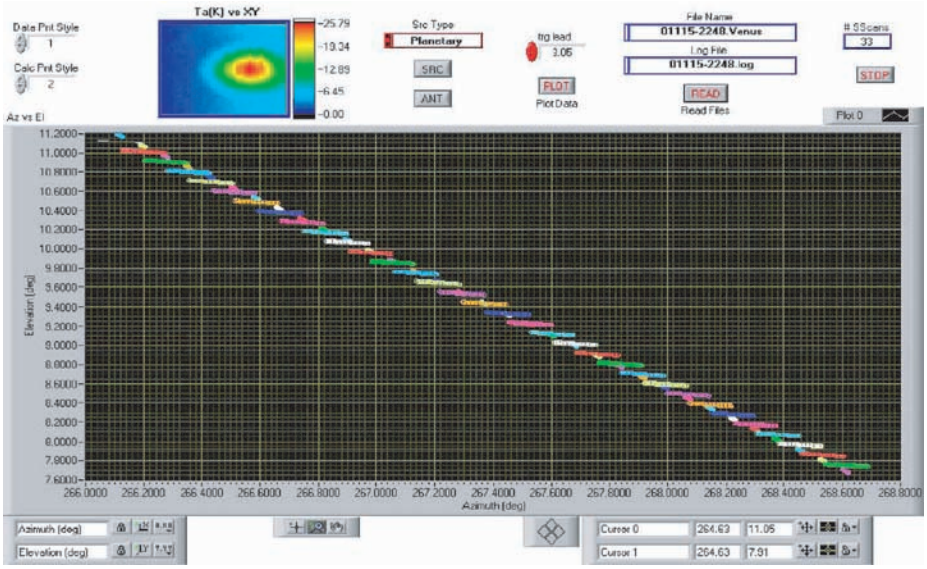

Fig. 7-4. Display showing a raster-scan performed at 13.8-GHz by TPR shown above, creating a 33 x 33 image of Venus as it sets.

1) The need to derive source size correction factor $C_r(\psi)$ is eliminated. However, one has the option to calculate $C_r(\psi)$ for various calibration radio sources using Eq. (7.4-6).
2) The need to derive accurate values of T_C for extended sources is eliminated. This is desirable because accurate derivations of T_C require mapping and deconvolving source structure from the antenna patterns, which change with antenna orientation (ψ). Using the OTF-mapping technique the accuracy of the antenna efficiency measurement is limited by the knowledge by which the calibration source flux density S_C is known.
3) The OTF-mapping system enables the experimenter to use compact point-like sources as secondary calibration sources for precision antenna calibrations. The vast majority of these radio sources are quasars, which are so distant that their angular sizes are very small. The problem is their radio brightness (flux density) values are highly variable so one must calibrate them against the handful of absolutely calibrated radio sources that are available. With few exceptions, the time-scales of the quasar variations are typically a few days, so flux density calibration measurements can be done rather infrequently, and relative measurements of antenna performance with azimuth and elevation can be done almost any time.

As a practical matter, the extended calibration source 3C274 (Virgo A) and the variable point source 3C273 serve admirably for such a strategy as they have nearly the same right ascension.

Substitution of Eq. (7.4-3) into Eq. (7.3-2) gives the result

$$T_p(\theta,\phi) = \frac{\eta A S_p}{2k} P_n(\theta,\phi) = T_p P_n(\theta,\phi) \tag{7.4-7}$$

so that the raster scan data set for the point source has a functional dependence determined by the beam pattern plus a background term due to the sky (in Eq. (7.4-9)), which may be linearly approximated over the small field scanned. Thus, if we assume that the antenna is in good alignment, there are small system aberrations, and the main reflector is nearly uniformly illuminated (which is a good approximation for the shaped reflector designs of the DSN), then $P_n(\theta,\phi)$ can be well approximated by an asymmetric Airy pattern

$$A\left(\kappa_\theta\theta,\kappa_\phi\phi\right) = \left[\frac{2J_1\sqrt{\kappa_\theta^2\theta^2+\kappa_\phi^2\phi^2}}{\sqrt{\kappa_\theta^2\theta^2+\kappa_\phi^2\phi^2}}\right]^2 \tag{7.4-8}$$

so that the system temperature data set for the point source raster scan has the form

$$T_{\text{op}}(\theta,\phi) = T_P A\left[\kappa_\theta(\theta-\theta_0),\kappa_\phi(\phi-\phi_0)\right] + T_{\text{op}} + a_\theta\theta + a_\phi\phi, \qquad (7.4\text{-}9)$$

where κ_θ and κ_ϕ are beamwidth parameters, θ_0 and ϕ_0 are the pointing errors, and a_θ and a_ϕ are the sky background coefficients for the θ and ϕ directions, and T_{op} is the system operating noise temperature.

The eight parameters appearing in Eq. (7.4-9) may be found from a nonlinear, least-squares fit [10] to the point-source raster-scan data, thus giving complete information on the peak temperature, and pointing errors and beamwidths for the two orthogonal directions corresponding to the scan axes. The precision of the resulting fit will depend on the noise fluctuations present in the noise temperature data, the scan parameters, and the data processing used, and these are dealt with in the following sections.

7.4.1 Fluctuations in System Noise Temperature

Three main sources of fluctuation of system noise temperature can be identified:

1) Thermal noise generated in the radiometer and atmosphere
2) Gain-bandwidth variations in the radiometer caused by ambient temperature fluctuations of electronic components, especially in the first stages
3) Fluctuations caused by variations in tropospheric density, especially of water vapor content. This is most significant at Ka-band.

In order to characterize and model the performance of the TPR, the two-sided power spectral density (PSD) was measured. The output fluctuations of a typical DSN Ka-band radiometer have been measured as a function of fluctuation frequency over the range 6.5×10^{-5} to 0.5 hertz (Hz), and the results compared with a model based on the above mechanisms. The results are shown in Fig. 7-5, where curve *a* corresponds to the radiometer looking at an ambient load and curve *b* was obtained with it looking at the zenith sky.

Curve *c* is a fit to curve *a* that is decreased by the square of the ratio of the system operating noise temperatures, $T_{\text{op}}\big|_{\text{amb}} \big/ T_{\text{op}}\big|_{\text{sky}} \cong 14.6$, and curve *d* corresponds to a statistical model for tropospheric fluctuations for average conditions at the DSN complex at Goldstone, California [11].

Curve *a*, which is constant at high frequencies and follows a $1/f^2$ dependence at low frequencies, corresponds to thermal noise and gain-bandwidth variations, and if these were the only terms present with the

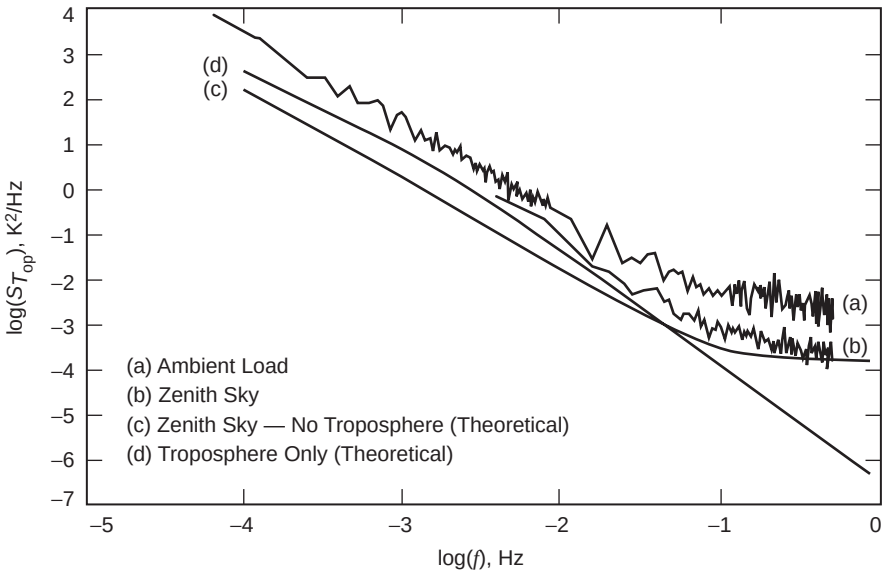

Fig. 7-5. Two-sided PSD of T_{op} fluctuations for a Ka-band radiometer.

radiometer looking at the zenith sky, the data of curve *b* would follow curve *c*. There is a significant departure from this; however, when curves *c* and *d* are added together, the result follows curve *b* closely. From this, we conclude that tropospheric fluctuations play an important role in the total radiometer fluctuations at frequencies below about 0.1 Hz.

Since we are interested in frequencies greater than 10^{-3} Hz when making gain calibrations, that is, times of interest are considerably shorter than 1000 s, we may consider only the high-frequency behavior of the Treuhaft-Lanyi model, which has a $1/f^{8/3}$ dependence so that curve *b* may be represented by the equation:

$$S_{T_{\text{op}}}(f) = S_0 + \frac{K_1}{f^2} + \frac{K_2}{f^{8/3}} \tag{7.4-10}$$

where the coefficients for the Ka-band radiometer tested have the values

$$S_0 = 1.50 \times 10^{-4}\,\text{K}^2/\text{Hz}$$
$$K_1 = 1.64 \times 10^{-6}\,\text{K}^2/\text{s}$$
$$K_2 = 2.36 \times 10^{-7}\,\text{K}^2/\text{s}^{5/3}$$

corresponding to average weather with the radiometer looking at the zenith sky and a T_{op} of approximately 100 K.

With the above form for the PSD of the fluctuations, one may determine the corresponding standard deviation of the fluctuations. This depends on the system operating temperature, T_{op}, the RF system bandwidth, B, the integration time, τ, used during the measurements, and, in view of the nonstationary behavior indicated by Eq. (7.4-10), the total duration of the measurement, T.

It can be shown that the variance of a random process, $X(t)$ of duration, T, having a high frequency cutoff, is given by

$$\sigma_X^2(\mathrm{T}) = 2\int_0^\infty \left[1 - \mathrm{sinc}^2(\pi f \mathrm{T})\right] S_X(f)\, df \tag{7.4-11}$$

where $\mathrm{sinc}(x) = \sin(x)/x$, and $S_X(f)$ is the two-sided PSD of the process. If the $X(t)$ signal is continuously averaged over a time interval τ, the resulting PSD is

$$S_{\bar{X}}(f) = \mathrm{sinc}^2(\pi f \tau) S_X(f) \tag{7.4-12}$$

so that the variance of the averaged process $\bar{T}_{\text{op}}(t)$, of duration T, is

$$\sigma^2_{\bar{T}_{\text{op}}}(\tau, \mathrm{T}) = 2\int_0^\infty \left[1 - \mathrm{sinc}^2(\pi f \mathrm{T})\right] \mathrm{sinc}^2(\pi f \tau) S_{T_{\text{op}}}(f)\, df \tag{7.4-13}$$

The evaluation of this integral for the spectrum given by Eq. (7.4-10) is accomplished by contour integration, with the result

$$\sigma_{\bar{T}_{\text{op}}}(\tau, \mathrm{T}) = \sqrt{\frac{S_0}{\tau} + \frac{2\pi^2 K_1}{3}\mathrm{T} + 18.3 K_2\, \mathrm{T}^{5/3}} \tag{7.4-14}$$

where it has been assumed that the measurement duration is considerably longer than the integration time, that is, T >> τ.

The duration of the measurement of interest in the raster scan method depends on the rate at which the data are taken, and the details of the analysis. For example, if one were to operate at a lower frequency than Ka-band, the $T^{5/3}$ term in the above equation, corresponding to tropospheric fluctuations, would be absent, and if a radiometer gain calibration were carried out at the conclusion of each line of the scan, then the appropriate time would be the time required for the execution of a single scan line. Generally speaking, however, T

will be the time required for one complete raster, and an important conclusion to be drawn from Eq. (7.4-14) is the need for *short* measurement times. This, perhaps counterintuitive conclusion, has been born out in actual tests, as will be shown below.

7.4.2 OTF-Mapping Research and Development System Design

The analysis carried out in Sections 7.3, 7.4, and 7.4.1, culminating in Eq. (7.4-5) expressing the aperture efficiency, η, as a function of the source temperature of a point source, demonstrates that the raster scan geometry and timing should be determined primarily by the need to accurately derive this quantity, T_p, and this question is discussed in the following.

Equation (7.4-14), together with the need to avoid settling problems with the antenna mechanical system, suggest that the raster scan should be performed with a continuous motion at a constant, high angular velocity in a given direction, say θ, while discontinuously stepping in the orthogonal direction, again, mimicking a TV scan (Fig. 7-4). This means that the data are taken "on the fly," hence the term, OTF-mapping. In so doing, the averaging process referred to above will contribute to a distortion of the signal that must be taken into account.

A second (and related) consideration is selection of the sampling interval t_s. In view of the Fourier transform relationship between the complex, far-field amplitude, $U_n(\theta,\phi)$, and the complex aperture field, $G(x,y)$, the scan signal for a single line of a point source is absolutely bandlimited.

Thus, for a coherent detection scheme such as that used in the microwave holography system [17,24], which also uses a raster-scan format, the signal is of the form $VU_n(\dot{\theta}t,\phi)$ where V is an arbitrary amplitude factor related to the antenna gain, and $\dot{\theta} = d\theta/dt$ is the constant scan angular velocity. The spectrum of this signal has, by virtue of the clearly defined antenna aperture, a sharp cutoff at $f_0 = \dot{\theta}/2\Theta_B$, where $\Theta_B = \lambda/2a \approx$ antenna main beam-width. This cutoff, moreover, is independent of the main reflector shape, illumination, and system aberrations; and it depends only on the maximum dimension of the aperture, d in the scanned direction.

Similarly, for the noncoherent (TPR) detection used in gain measurements, the signal is of the form

$$VP_n\left(\dot{\theta}t,\phi\right) = V\left|U_n\left(\dot{\theta}t,\phi\right)\right|^2 \tag{7.4-15}$$

so that its spectrum is given by the autocorrelation of the coherent spectrum, and consequently has a cutoff frequency twice as high.

From the above, we infer that Nyquist sampling for a coherent system requires a minimum of one sample per beamwidth; while for a noncoherent system, a minimum of two samples per beamwidth is required. Also, since the signal spectrum is bandlimited in both cases, a sharp cutoff digital filter can be used to remove noise above the cutoff, and this can then be followed by a suitable Wiener filter to compensate for the distortion introduced by the integration, with minimal loss of high-frequency information.

Figure 7-6 shows a schematic block diagram of the antenna calibration OTF-mapping research and development (R&D) system. It can calibrate any of the DSN antennas via interfaces to their antenna controller, encoders read out, and diodes and microwave controls. All the interfaces must be done locally at the antenna under test (AUT). The system achieves high accuracy of raster alignments by the virtue of interfaces to the antenna angle encoders, which are being read at a high speed of 1000 readings/s. An internal computation engine in the data acquisition converts the sidereal motion of radio sources from right-ascension declination (RA-DEC) to antenna coordinates in azimuth-elevation (AZ-EL) in real-time, allowing for a tight feedback loop control of synchronizing receiver triggering (TPR) to the antenna position.

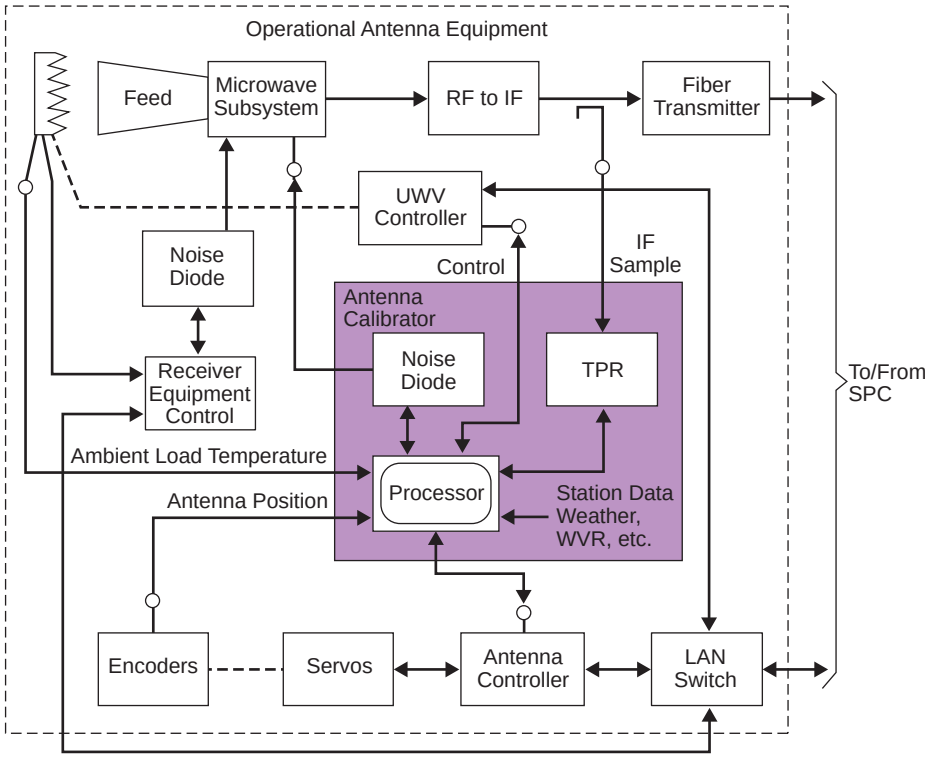

Fig. 7-6. OTF-mapping (raster-scan) R&D system, in shaded area showing interfaces to any DSN antenna (UWV = microwave).

The first trigger position in each of the raster subscans is determined by position synchronization, while the remaining data are triggered via time synchronization locked to the internal system clock. As a result, one of the critical elements of this design is the need to maintain a constant, known angular velocity of antenna motion during the taking of data along a given direction. The TPR is sampled at a constant known rate so that the relative position at which the data are taken is known with high accuracy; and thus, antenna-settling time is no longer an issue. This design ensures the alignment of the individual subscans within the full raster. The OTF–mapping R&D data acquisition algorithms include the computation of the radio source positions such that at any given time the position of the antenna relative to the source is known. Since the data are taken "on the fly," the integration occurring during the sampling interval results in an attenuation of high-frequency information ("smearing"), but this can be recovered by an inverse filtering process (Wiener filter). Since the source is scanned in a raster-type pattern by stepping from line to line, a complete data set corresponding to a complete raster contains all of the relevant data and not just a sampling of it along two orthogonal directions. This means that one is effectively including all of the source radiation so that no source-size correction is necessary (Eqs. (7.4-5) and (7.4-6)). The resulting three-dimensional (3-D) data set is then used to determine, by means of least-squares fitting, the main beam pattern, from which, the relevant calibration parameters are directly determined.

Figures 7-7 and 7-8 show the real-time display of the OTF-mapping R&D data acquisition instrumentation display for the two-dimensional (2-D) and 3-D cases, respectively. In both cases Eq. (7.4-9) is solved using the Levenberg-Marquardt method to determine the non-linear set of coefficients of these equations, which minimizes a chi-square quantity. In Fig. 7-7, the white dots

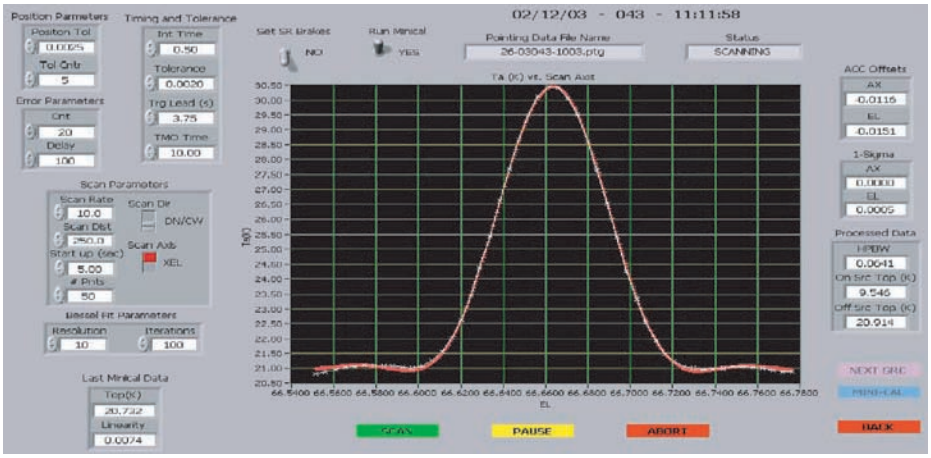

Fig. 7-7. OTF-mapping R&D data acquisition real-time display.

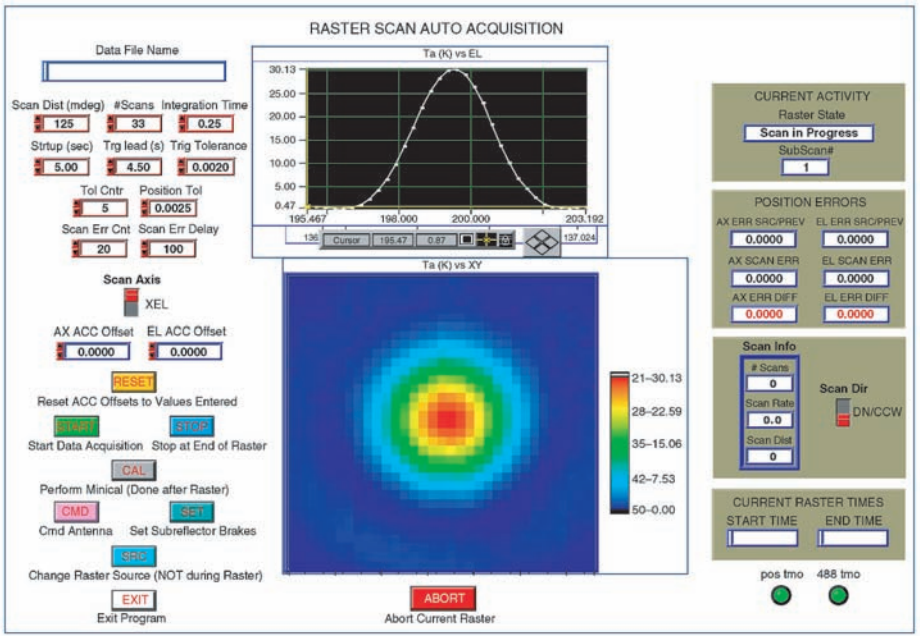

Fig. 7-8. Real-time display of the OTF-mapping R&D instrumentation during the acquisition of a 3-D raster.

are the raw data, and the red line is the fitting Airy function. Figure 7-8 shows the real-time display during the acquisition of 3-D raster (middle color plot), while individual subscans are shown above in white over black plot. In both cases, the precision in the estimation of the equation parameters are determined from the diagonal elements of the covariance matrix and also displayed in real-time for parameters of interest. Figure 7-9 shows the main panel program of the R&D OTF-mapping R&D system.

In order to study the interaction between scan velocity, $\dot{\theta}$, array size, N, and integration time, τ, computations have been made of the errors expected in the fitted parameter T_p for a range of values for each of these parameters for a one-dimensional fit corresponding to a single scan line, and the results are shown in Table 7-1. In Table 7-1, rms background noise from a single scan line, σ_l, and complete raster, σ_r, are computed for given scan line duration, t_l, and raster duration, t_r, from a model based on the measured power spectral density for the radiometer system. In all cases, the sampling interval, $t_s = \tau/2$. The computed errors in T_p are based on a general, nonlinear least-squares fitting analysis, using Eq. (7.4-14) to estimate the noise standard deviation, and a Gaussian beam pattern rather than an Airy pattern, for simplicity.

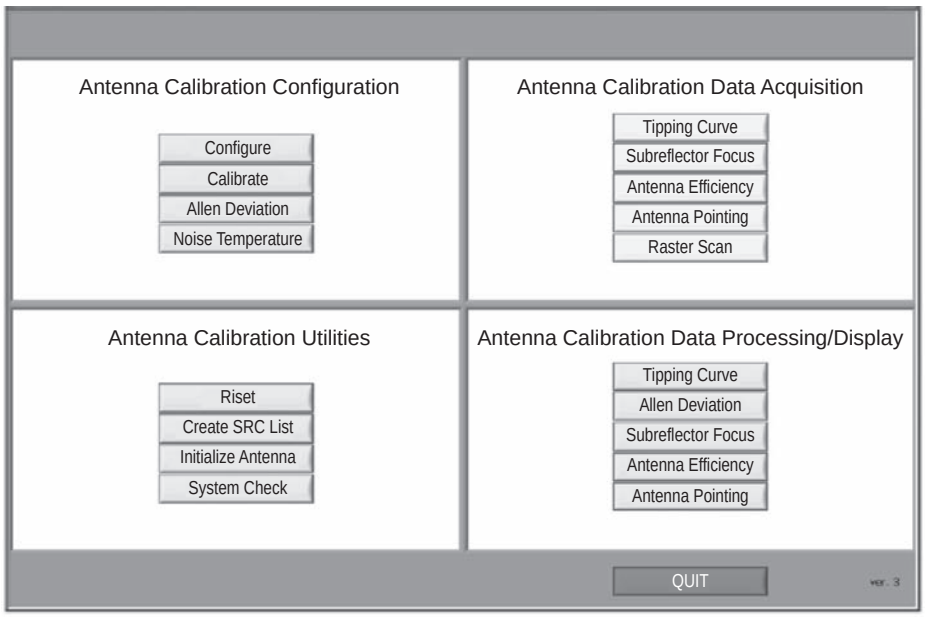

Fig. 7-9. OTF-mapping R&D main program panel.

Also shown in Table 7-1 are the rms fitting errors of aperture efficiency versus elevation curves based on quadratic fits to the data for a complete 6-hour pass of the source. These errors are inversely proportional to $\sqrt{N_r}$, where N_r is the number of complete rasters executed during the pass, each of which yields an estimate of all of the fitting parameters.

$$T_P(\theta) = T_P \exp\left[\frac{-\kappa_\theta^2(\theta-\theta_0)^2}{2}\right] \tag{7.4-16}$$

7.4.3 Test Results

Field test results agree very closely with the computed performance predictions presented in Table 7-1. As a typical example, an observation of Venus with the following parameters (see Fig. 7-10):

Source: Venus

Raster size: 33 × 33

Total measurement distances: 125 × 125 millidegrees (mdeg)

τ = 0.25-s

Scan velocity = 15.6-mdeg/s

Total measurement duration = 430-s

Table 7-1. Theoretical simulation errors for the source temperature, and aperture efficiency η(ψ) versus elevation curve, as a function of the scan velocity, array size, N, based on nonlinear least-squares fitting analysis for raster scan data acquired with 34-m antenna at Ka-Band with an elevation of 90 deg and with a troposphere retrace time of 2 s.

τ(s)	t_l(s)	t_r(s)	$\dot{\theta}$(m deg/s)	$\sigma_l(K)$	$\sigma_r(K)$	$\sigma_T(K)$	$\bar{\sigma}_{FIT}$(%)	N_r
				$N = 17$				
0.1	0.8	47.6	100	0.036	0.068	0.037	0.042	453
0.2	1.6	61.2	50	0.026	0.074	0.041	0.052	352
0.4	3.2	88.4	25	0.019	0.094	0.052	0.080	244
0.8	6.4	142.8	12.5	0.017	0.136	0.075	0.147	151
1.6	12.8	251.6	6.24	0.022	0.214	0.118	0.309	85
				$N = 33$				
0.1	1.6	118.8	50	0.037	0.123	0.034	0.060	181
0.2	3.2	171.6	25	0.027	0.159	0.044	0.095	125
0.4	6.4	277.2	12.5	0.026	0.232	0.064	0.176	77
0.8	12.8	488.4	6.24	0.024	0.369	0.101	0.370	44
				$N = 65$				
0.1	3.2	338.0	25	0.038	0.275	0.038	0.115	63
0.2	6.4	546.0	12.5	0.029	0.405	0.055	0.215	39

Encoder sampling rate = 1000/s

TPR sampling rate = 150/s

The peak temperature was obtained by fitting the data to a 3-D Airy function, which resulted in 1-sigma error of 0.085 K. This result is very much in agreement with the predictions computed in Table 7-1.

The system also computes the reduced chi-square such that if high values are computed, it can be concluded that a main source of the error is due to the fact that the fitting function cannot follow the data to within the limit imposed by the random data errors. In field measurements, we found out that indeed this is the case when the antenna sidelobes are asymmetric as would be due to poor subreflector alignment.

7.5 Blind-Pointing Calibration

The OTF-mapping R&D system also proved itself capable of providing a new record of best blind-pointing performance, which was achieved on the DSN 34-m BWG antennas. In doing so, two new technologies were used:

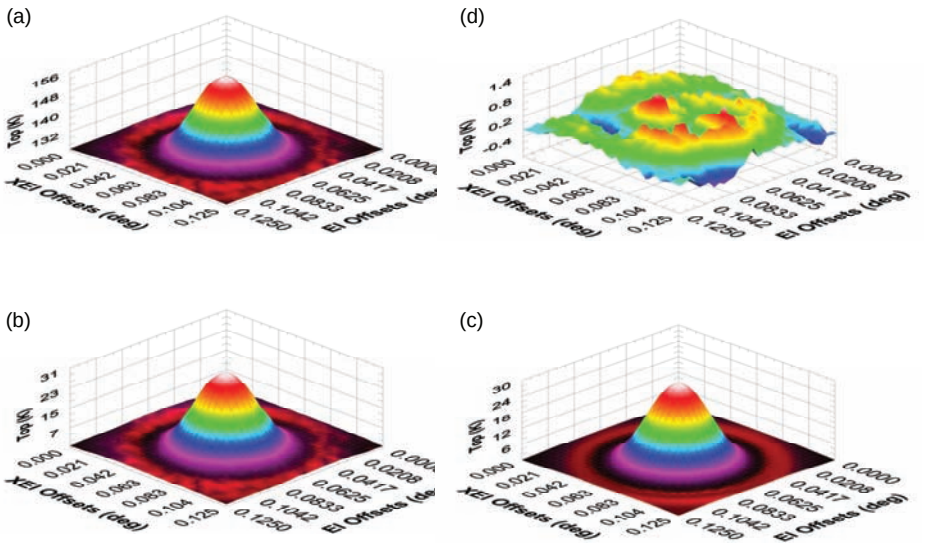

Fig. 7-10. Screen image displaying error analysis for a full 3-D raster scan indicates that an accuracy of 0.1 K was achieved in determining the source peak temperature: Top left: Raw data. Bottom left: Raw data after removal of background and slope. Bottom right: Fitting function to raw data on bottom left. Top right: Map-differencing between raw data and fitting function.

1) The OTF-Mapping R&D system [12] and
2) New 4th order pointing model software [14].

The 4th order pointing model was devised as a result of noticing systematic error residuals remaining in the data after applying the conventional 1st order model. The 1st order model, which typically has six to eight mathematical terms (Fig. 7-11), is a physical model originally developed by Peter Stumpff and published in "Astronomical Pointing Theory for Radio Telescopes" in 1972 [23]. The 4th order model (Fig. 7-12) was derived by expanding the spherical harmonics that are related to the associated Legendre polynomials by Eqs. (7.5-1) and (7.5-2) below, to the 4th order, resulting in 50 mathematical terms:

$$Y_{lm}(\theta,\phi) = \sqrt{\frac{2l+1(l-m)!}{4\pi(l+m)!}} P_l^m \cos(\theta) e^{im\phi} \tag{7.5-1}$$

where,

$$P_l^m(x) = (-1)^m \left(1-x^2\right)^{m/2} \frac{d^m}{dx^m} P_l(x) \tag{7.5-2}$$

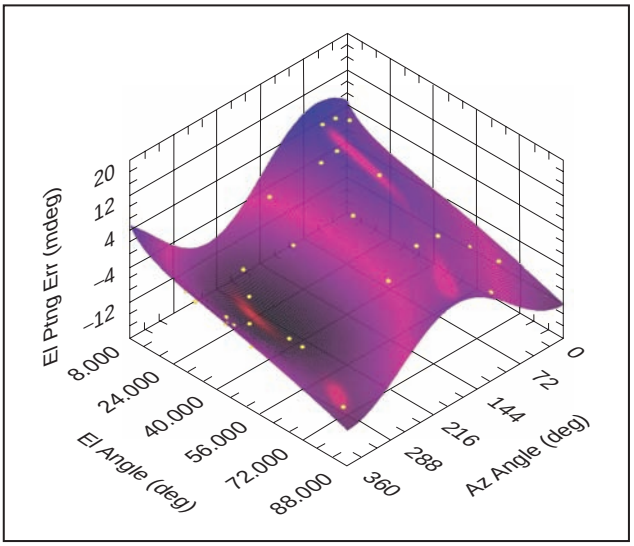

FIg. 7-11. Traditional 1st order pointing model resulting in a predicted performance of 2.74-mdeg MRE.

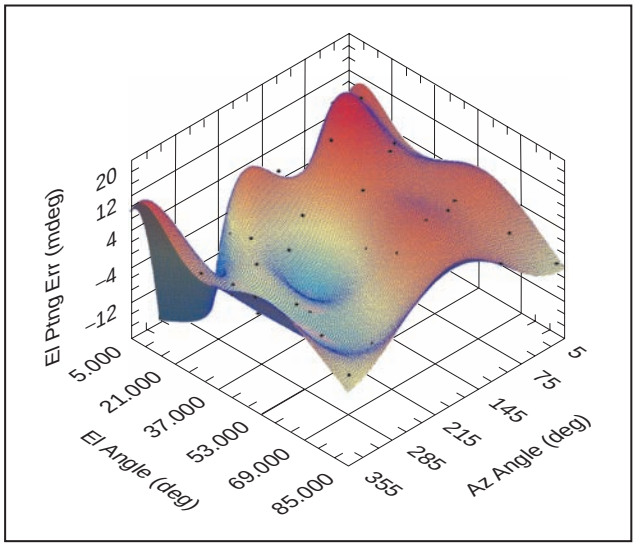

FIg. 7-12. New 4th order pointing model resulting in a predicted performance of 1.49-mdeg MRE.

All the physical terms from the 1st order model that did not appear in the expansion were retained in the new model, resulting in a total of 59 mathematical terms. As shown in Figs. 7-11 and 7-12, the application of the new 4th order model reduces the predicted mean radial error (MRE) by a factor

of approximately 2. Additional field tests confirmed that the blind pointing performance improved by approximately a factor 2–3 relative to the 1st order model.

To facilitate an efficient all-sky survey for the observation of radio sources, a scheduling program was written and integrated within the OTF-mapping R&D system. Fig. 7-13 is the output produced by the scheduling program for DSS-13, where each (yellow) dot represents a radio source to be observed and data recorded utilizing a 2-D cross-scan as illustrated in Fig. 7-7. The gathered data are then processed by the 4th order pointing model software that computes a new pointing model for the antenna. For now, we only want to present the final proven results. When the derived model was applied to the DSS-26 BWG antenna at Goldstone, California, and used in operational activity to track Voyager I, a new record of performance level of 3.5-mdeg mean radial error (MRE) was achieved, that was previously never attained on any of the 34-m BWG antennas (typical performance level of these antennas was 7–10 mdeg MRE at best). The result of this track is presented in Fig. 7-14.

What else is special about the data distribution of Fig. 7-14 is that in addition to the low MRE value, the data have a zero mean. This is particularly interesting, because in prior residual pointing error data plots, a sharp transition was observed as spacecraft moved across the meridian. This result was helpful in helping diagnosing the cause of that hysterisis and attributing it to an elevation encoder coupler [15].

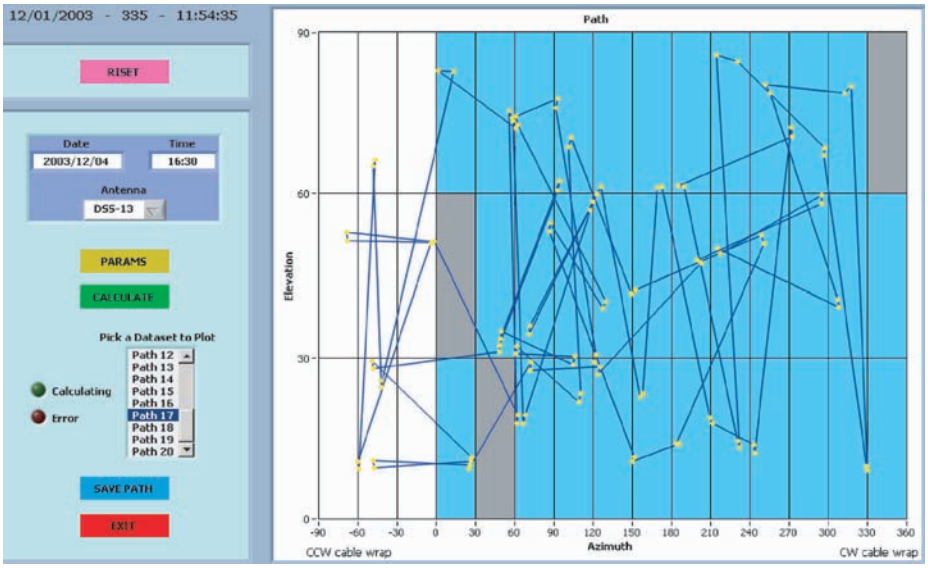

Fig. 7-13. OTF-mapping R&D scheduling display for efficient all-sky source selection and observation (CW is clockwise and CCW is counterclockwise).

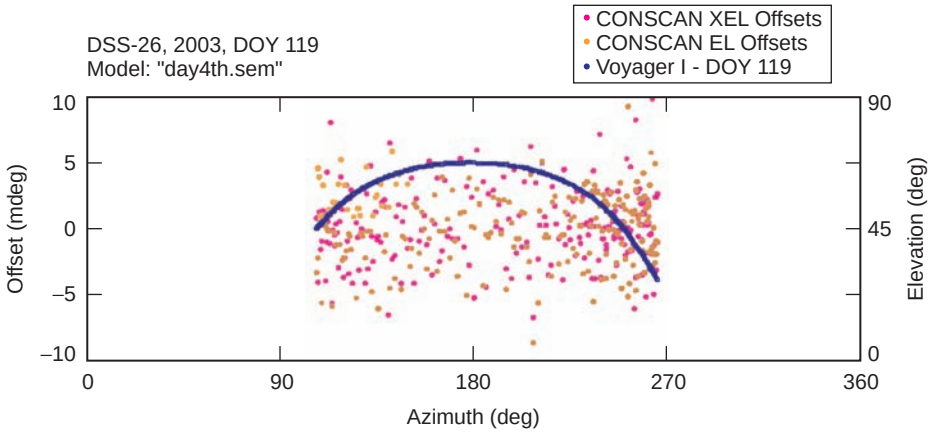

Fig. 7-14. DSS-26 tracking Voyager I (2003, DOY 119) with 3.5-mdeg MRE using 4th order model ("day4th.sem").

7.6 Cassini-Jupiter Microwave Observation Campaign (Cassini JMOC)

7.6.1 Introduction

The objectives of the Radar Instrument on board the Cassini-Huygens spacecraft are to map the surface of Titan and to measure properties of Saturn's rings and atmosphere. However, utilizing the Cassini radar as a radiometer can provide invaluable information regarding the atmosphere and surface compositions of Saturn and its moons, as well as Jupiter. However, the fact that the Cassini-Huygens onboard radar was not calibrated as a radiometer prior to launch was a deterrent for making such high-accuracy measurements. The flyby of the Cassini-Huygens spacecraft past Jupiter in December 2000 provided an opportunity to calibrate the onboard radar as a radiometer utilizing Jupiter as its known temperature load. The accuracy with which Jupiter's disc temperature could be determined from ground observations would translate directly to the accuracy of the calibration of the onboard radiometer; and consequently, it would determine the accuracy with which atmosphere and surface measurements of Saturn and Titan can be made. The fact that the Cassini onboard radar operates at 13.78 GHz was an additional challenge since none of the JPL-DSN ground antennas was equipped with a feed at this exact frequency.

In a presentation made to the principal Investigator (D. Rochblatt, presentation to Mike Klein and Mike Janssen, dated May 7, 1999), the strategy for the measurements and calibrations was laid out. The goal was to measure Jupiter's disk temperature with a 1-sigma accuracy of 2-percent, which if it

could be achieved, would enable new science. The technique is based on performing high-accuracy ground-based calibration measurements simultaneously with the spacecraft observations and at the exact same frequency of 13.78 GHz. This allows us to transfer to the Cassini radar receiver the ground-based radio astronomy flux calibration with high accuracy, using Jupiter as a common reference source. What made this calibration challenging is the fact that absolute calibration measurements of radio sources near 13 GHz did not exist. Current estimates of the absolute uncertainty of the radio astronomy flux calibration scale tend to increase with frequency in the centimeter-to-millimeter radio astronomy bands. Typical estimates of systematic errors in radio source flux measurements near 5 GHz are ~2 percent (1-sigma), whereas the estimates near 22 GHz are ~10 percent (one-sigma).

To achieve the maximum accuracy, a ground based TPR (Fig. 7-3) was designed, built, and installed at DSS-13, 34-m BWG R&D antenna (Fig. 7-2), while incorporating the OTF-mapping R&D system technique described above. After the installation of the TPR, and to support these in-flight calibrations, a coordinated series of ground-based observations named the Cassini-Jupiter Microwave Observing Campaign (Cassini-JMOC) was carried out from November 2000 through April 2001.

The second objective of the Cassini-JMOC project included an educational component that allowed middle-school and high-school students to participate directly in the ground-based observations and data analysis. The students made their observations as part of the Goldstone Apple Valley Radio Telescope (GAVRT) project.

7.6.2 Observations

The 34-m GAVRT antenna was used to participate in a multi-frequency campaign to study Jupiter's synchrotron radiation [16]. GAVRT students and teachers teamed with professional scientists and engineers to measure the ratio of Jupiter's flux density relative to those of six calibration sources that were selected to mitigate different sources of random and systematic errors. The calibration source selection criteria included the following:

- Flux density greater than 2 Jy to ensure high signal-to-noise ($5 < SNR < 10$) for individual measurements.
- Spectral Index is *known* with sufficient accuracy to interpolate the flux density at 13.8 GHz.
- Angular size should be small compared to 0.041 deg (the 3-dB width of the 34-m antenna beam at 13.8 GHz).

The source 3C405 (Cygnus A) was *exempted* from these selection criteria because it is one of the sources that was also being measured directly from Cassini during special calibration sequences in the fall of 2000 and other times during the mission. There is evidence that the source does not vary with time

and that its circular polarization is small (4 percent). Its proximity to Jupiter in the sky (right ascension and declination) was an advantage. All measurements of Jupiter and the calibration sources were processed to remove sources of error caused by changes in system performance with antenna tracking in azimuth and elevation. System "mini-cal" sequences were performed about three times per hour to monitor subtle changes in receiving system gain, stability and linearity.

7.6.3 Results

Tests were conducted in April 2001 at DSS-13 using the OTF-mapping R&D instrumentation to observe Venus, Jupiter, 3c405, 3c273, 3c274, 3c286, NGC7027, 3c123, and 3c84. Given that the antenna half power beamwidth (HPBW) for the 34-m antenna operating at 13.8 GHz is approximately 0.041 degrees, the raster dimensions were scaled for approximately three times the HPBW to produce maps with spatial dimensions of 0.125 × 0.125 deg on the sky. The temporal resolution along the scan corresponded to about 1/10 HPBW (approximately 0.004 deg), which resulted in data arrays of 33 × 33 points (Fig. 7-8). Typical raster-scans required 15–20 minutes to complete. When the weather was calm, excellent raster alignment was achieved. However, when the wind speed was above 16 km/hr (10 mph) apparent misalignments in the raster were observed (see Fig. 7-15, the raster data at 34.3-deg elevation). The source of this problem is believed to be sub-reflector oscillations because no apparent misalignment in the antenna angle encoders registering was noticed.

In deriving the DSS-13 antenna efficiency, the OTF-mapping R&D system was used tracking 3c273 (point source) and 3c274 (calibrated source) near the rigging angle of 49 deg, where an efficiency of 61 $\pm$2 percent was computed. Then the OTF-mapping data of Venus obtained from 8.7- to 58-deg (Fig. 7-15) elevation was also calibrated at 49-deg elevation to that value. In the process, a source size correction of 1.070 was computed for 3c274 near the same rigging angle, which compares well with the independently derived value of 1.075, obtained using the other scanning techniques that required many more observations.

The data and the plots demonstrate the capability of the OTF-mapping R&D system to reveal distortions in the antenna beam pattern at low elevation angles as is clearly shown at 8.7- and 12.7-deg elevations. These distortions are

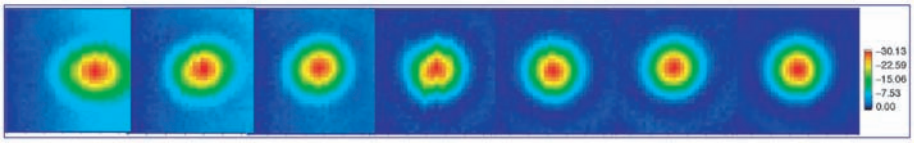

Fig. 7-15. A series of patterns taken of Venus at source elevations from 58 deg to 8.7 deg.

due to gravity-induced deformation of the main reflector surface [17]. At 8.7 deg, the antenna pointing error causes the image to be off center. The mispointing of the antenna is due in large part to errors in estimating the refraction correction at such a low elevation angle.

Figures 7-16(a) and (b) illustrate the stages of data processing for the OTF-mapping R&D system. Figure 7-16(a) shows the 3-D response of the raster

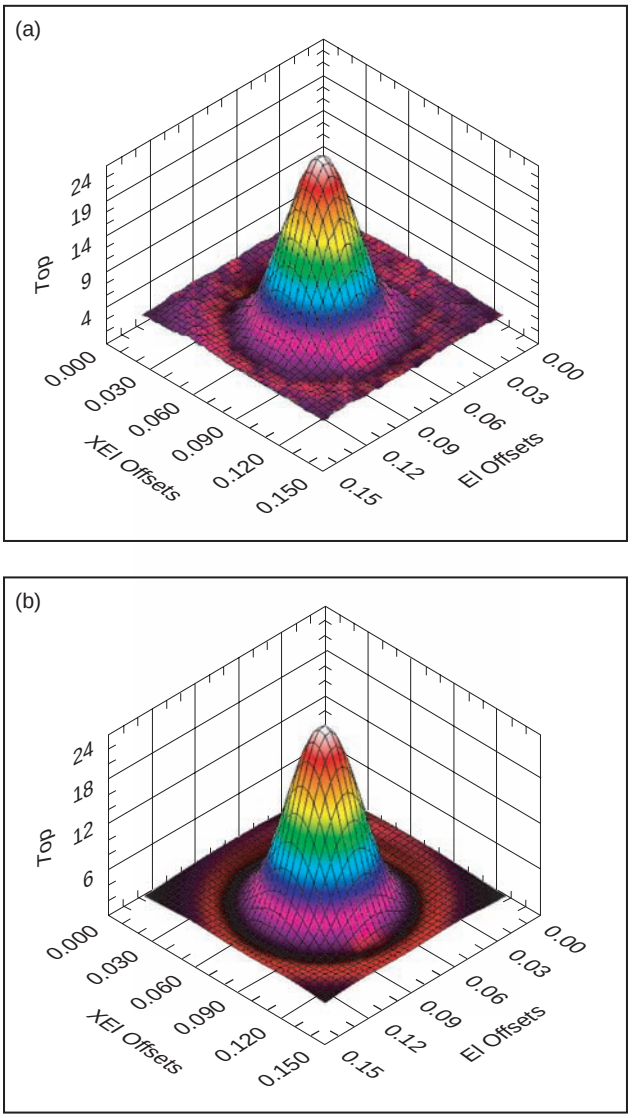

Fig. 7-16. Stages of data processing for the OTF-mapping R&D system, including (a) 3-D response from Venus and (b) fitting of raw data with an Airy function. (XEL is cross elevation).

scan data taken across Venus when it was near 58-deg elevation. The plot was constructed after removing the background noise, which is fitted to a two-dimensional baseline with arbitrary slope (Eq. (7.4-9)). Venus was close to Earth; and therefore, it was a very strong radio source when the measurements were made. Consequently, the noise level in the map is very low, and the smooth surface of the 3-D plot indicates the excellent alignment of the individual raster sub-scans. The x and y-axis coordinates correspond to elevation (El) and cross elevation (XEl) of the maps. The samples along sub-scan direction are approximately 0.0039 deg. The z-axis shows the measured system noise temperature in kelvins.

Figure 7-16(b) is the result of fitting the raw data with an Airy function (Eq. (7.4-8)). The mathematical expression that describes the spatial smoothing is caused by diffraction when radio waves (or light waves) are reflected off a circular aperture, which in this case is the 34-m effective-parabolic dish. The formal equation for diffraction of radio antennas is the Jacobi-Bessel series expansion of the far-field pattern of the antenna.

Figure 7-17 shows the data processing of OTF-Mapping data of 3c405, Cygnus A, using DSS-13. Since 3c405 is an extended source for this antenna at 13.8 GHz, the convolution of the source with the antenna main-beam resulted in the image on the top and lower left of Fig. 7-17. (The lower left of Fig. 7-17 is derived after the removal of the atmospheric component contribution to the noise temperature). The lower right corner of this figure displays the Airy pattern model of the antenna main-beam. After the subtraction of the main-beam from the data, the double-lobed shape of Cygnus A is revealed. A VLBI image of Cygnus A taken by the VLA is shown in Fig. 7-18 for reference. The criticality of a 3-D raster-scan for accurate determination of source size correction is clearly demonstrated by this process.

The observed ratios of Jupiter to the six calibration sources were used to calculate the effective disk temperature of Jupiter from each calibrator. The spectral indices of Venus and the sources 3C286, 3C123, and NGC 7027 were updated with new results from the National Radio Astronomy Observatory (NRAO). The result is shown in Fig. 7-19. The average disk temperature was computed to be 165 K ±2 K. This signifies an accuracy of 1.2 percent, which exceeds the project goal. This accuracy translates directly to the accuracy with which the Cassini Radar can be used as a radiometer to study the atmosphere and surfaces of Saturn and its moons. Most notable, these results were possible due to the new set of observations carried out at Goldstone to map the brightness distribution of 3C405 and 3C274 using the OTF-mapping technique described above. If these observations had been made by conventional auto-bore measurement techniques, an accuracy of only 4.3 percent would have been achieved [18].

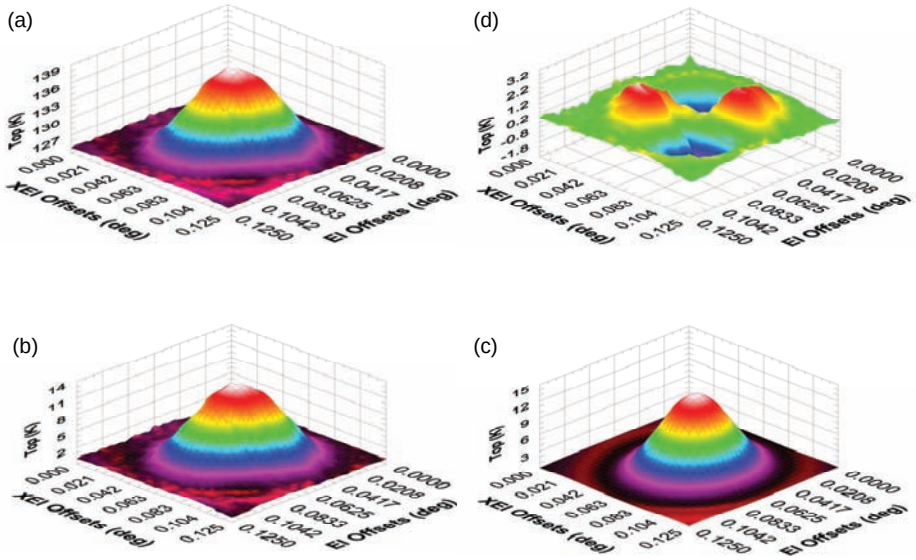

Fig. 7-17. 3c405, Cygnus A mapping by a single 34-m antenna at 13.78 GHz.

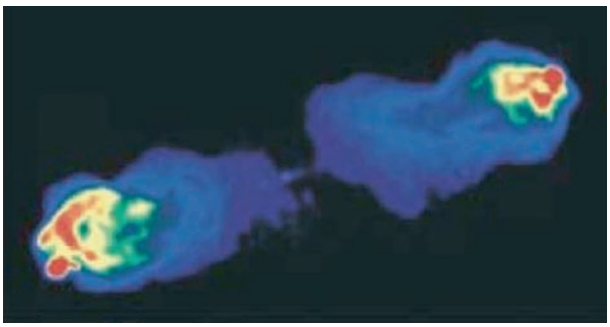

Fig. 7-18. Cygnus A image courtesy NRAO/AUI/NSF
Investigator: R.A. Perly.

The raster scan technique reduces the uncertainty in the total flux density measurement that arises when the antenna beam partially resolves the spatial dimensions of an extended radio source.

7.7 Operational Antenna Calibration & Measurement Equipment (ACME) for the DSN

The OTF-mapping R&D system provided a complete functionality in a portable package; however, it did not provide the best architecture suitable for an operational DSN environment. It was desired to have an antenna calibration system that could provide all these functionalities from the centralized DSN

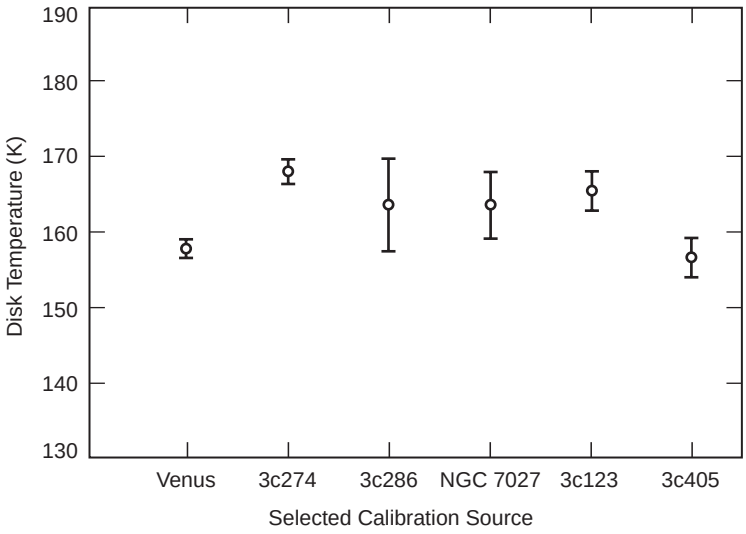

Fig 7-19. Jupiter disk temperature determined by OTF-mapping technique. (Data in the figure were taken with an accuracy of 1.2 percent, a Jupiter disk temperature of 165 K, and an observation frequency of 13.8 GHz.)

Signal Processing Center (SPC) and interfacing it to the Network Monitor and Control (NMC) of the DSN subsystem. ACME [25] was designed to run over the SPC-LAN automating these procedures using standard monitor and control without modifying operational environments.

The other key design feature of the operational system that is different from its R&D predecessor is in its synchronization implementation. While in the R&D system synchronization is based on position and timing (Section 7.4.2 above), ACME synchronization is based on time alone. The time synchronization is provided by computing a predict file for the antenna controller, which describes the exact antenna positions relative to the radio sources during a complete raster (for either the 2-D or 3-D scans) as a function of absolute time. These time stamps within the predict file provide the synchronization with the radiometer recorded values. A block diagram of ACME interface in the DSN environment is shown in Fig. 7-20.

7.7.1 ACME Major Capabilities

ACME uses noise-adding radiometer techniques to compute system noise temperature (SNT) values that can be used to compute pointing offsets and antenna efficiency and subreflector optimization for different feeds.

The two channels provided with the system, enable simultaneous measurements of two frequency bands, or two polarizations in the same band. This feature is especially useful in determining antenna beam coincidence at

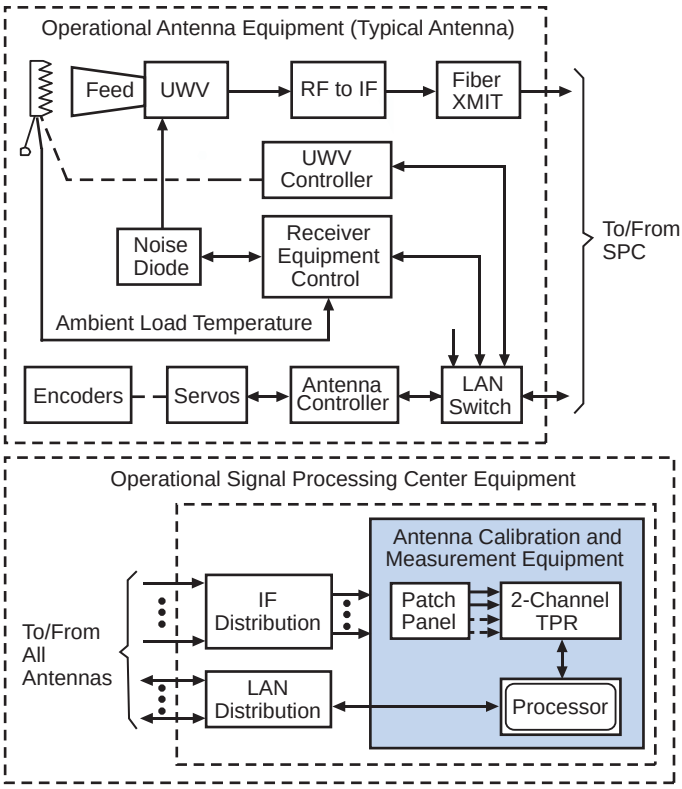

Fig. 7-20. ACME system block diagram.

different frequency bands and greatly improves productivity of time devoted to calibration. The new system can be used to evaluate non-modeled phenomena such as coupler hysteresis (el or az different readings at same position coming from different directions), and weather affects on antenna pointing performance. Surface deformations caused by temperature gradients and strong wind and bad refraction correction can be examples of weather interference in antenna pointing performance. In addition the system can be used to measure the antenna track level unevenness, and detection of servo anomalies. The system provides for the maintenance of pointing models from previous observations, for refining accuracy and provides general archive of observation data, for trend and historical data analysis.

7.7.2 Subsystem Design and Description

ACME is designed to perform the calibration activities by interfacing with the existing resources at the station and measuring the noise power with a square-law power meter. A single equipment rack is installed at each SPC that interfaces with the antenna servo, the microwave switches, the noise diodes and

the antenna controller through “predict” distribution. The software uses current communication protocols used on the DSN SPC LAN.

The calibration activities are performed without changing the station operational configuration. This dramatically reduces the risk over the subsequent spacecraft tracking passes. The preparation time is small enough to allow making use of virtually all antenna free times to obtain usable data. More calibration data will be available in the next years to increase the knowledge over the station calibration status, the degradation rates, and a number of hitherto unknown factors that impact the pointing accuracy and efficiency of the antenna.

The power measurements are being carried out by a set of band-limited filters of 5-percent bandwidth (BW) and using broad-bandwidth square-law detectors. Signals from the complex interface (IF) switch distribution allow for selecting any front end, and can be applied to either a 250-MHz (BW = 12.5-MHz) center frequency, 321-MHz (BW = 16-MHz) center frequency, or a tunable filter from 200 to 400 MHz (BW = 5 percent).

ACME uses noise adding radiometry (NAR) [19] techniques with the 50-K diode to calibrate operational parameters. The process is highly automated and does not require any manual intervention for configuration. The radio source catalog from year 2000 is maintained within the system; and it computes nutation, precession, and diurnal and annual aberration to determine current position and build cosine director type of “predicts” for later antenna controller distribution and synchronization. When executing continuous scans, the width of each scan is typically set to as much as five times the HPBW over the source. The system radiometer measures and integrates noise power to derive a far-field antenna pattern over a calibrated rectangular coordinate system, normally, elevation versus cross-elevation.

7.7.3 Radiometer Calibration

Power measurements are derived by switching a 50-K diode as reference over ambient load and sky in a NAR [20,21] mode. Microwave switch configurations, as well as diode modulating control signal, are fully automated under ACME control. The precision achieved during measurement of total power is 1 percent, and while operating in a NAR mode it is 1.2 percent.

7.7.4 Pointing Measurements

As of today, pointing is the main application of ACME. As DSN moves up its operating frequency, pointing precision becomes more and more relevant.

The calibration system must maintain systematic error models and is able to collect data in a variety of conditions without interfering with the DSN operations schedule. ACME performs these functions, and it is able to give an

overall picture of pointing quality in less than 5 hours under normal weather conditions.

ACME is operated with a user friendly graphic user interface (GUI). Clicking over a source on the general source display map, causes the given source to be included in the source list for a given session observation. The "predicts" are built for the sources on the list for later distribution to antenna controllers which, will direct antenna movements to scan the sources.

The main computations engine of the system is based on a nonlinear Levenberg-Marquardt regression using Eqs. (7.4-8) and (7.4-9) from which SNT values are derived from measured data.

The composition of the two-axis (El and Xel) scan gives the basic data to the system for calibration. The center of the scan is the theoretical position of the radio source. From the distance of the maximum noise power relative to the center of the scan, the position error of the antenna in the measured axis is computed. The base line of the noise is the background noise, so the curve T_{op} is the source temperature measured with the antenna. If the source is an accurately modeled radio source, the antenna efficiency can be derived from this measurement. The width of the curve at the –3-dB level is the main beam HPBW.

Data derived from computed offsets are used to derive either first- or fourth-order systematic error models. ACME provides a model calculator that can read data from the system or other sources. In addition, it provides an input filter to apply to input data. Another feature is the ability to "fill" empty areas of the sky with data from previously built models.

7.7.5 Subreflector Optimization

Subreflector misalignment translates into antenna efficiency loss. The Ruze equation gives an expression for this loss:

$$\eta = e^{-\left(\frac{4\pi\varepsilon}{\lambda}\right)^2} \tag{7.7-1}$$

where ε is proportional to the subreflector displacement [22].

To determine the optimal subreflector position, ACME determines the maxima of the curve derived from the subreflector movement over the selected axis. Two orthogonal scans are performed for every position.

The equation used to calculate loss of efficiency derived for small pointing errors is:

$$T = T_0 \cdot e^{-\left(\frac{2.273\cdot\theta^2}{HPBW^2}\right)} \tag{7.7-2}$$

7.8 Conclusions

A theoretical analysis of gain and pointing calibration methods, together with a realistic assessment of system noise characteristics, has led to the conclusion that significant improvement in performance can be realized by performing rapid, continuous raster scans of point and extended radio sources, and by determining temperature and pointing information from two-dimensional, nonlinear, least-squares fits of the data to realistic beam patterns.

The method has the further advantage that source-size corrections, which presently represent a significant source of error in both gain measurements and source flux-density determinations, are not needed since essentially all of the source flux density is collected during the raster scan.

The use of rapid scanning also results in the collection of vastly more data than with conventional techniques, so that errors in gain, or aperture efficiency versus elevation curves can be greatly reduced.

Measurements at Ku-band and Ka-band, based on 2-D and 3-D fitting are in good agreement with theoretical calculations using measured power spectral density data to predict the background noise during a scan, and using this background noise as input to a nonlinear, least-squares model to predict fitting parameter errors.

This application of the OTF-mapping R&D system for the Cassini-JMOC calibration work demonstrates some of the valuable attributes of the system for the calibration and performance analysis of the DSN antennas for telemetry and for radio science.

The OTF-mapping R&D system has been developed into an operational antenna calibration and measurement equipment (ACME) system. ACME initial delivery is the first step in an ambitious project to provide the DSN with a standard calibration tool. This is the first attempt to use a unified evaluation criterion, allowing larger quantities of data to be collected and improving its quality. It will allow the technical community to know the state and evolution of all antennas via a common database. Set up of the tool is quick and operationally safe. Calibration times depend on the type of measurements, but experience gathered so far indicates that it will easily be made compatible with DSN routine maintenance and operations.

As the system is used by the calibration engineers at the stations, more feedback is expected and more and better improvements will be added to the future work.

References

[1] J. Bautista, R. Clauss, S. Petty, and J. Shell, "DSN Low Noise Amplifiers In the New Millennium," *JPL-TMOD Technology and Science Program News*, vol. 82, no. 5, January 2001.

[2] L. W. M. Baars, R. Genzel, I. I. K. Pauliny-Toth, and A. Witzel, "The Absolute Spectrum of CasA: An Accurate Flux Density Scale and a Set of Secondary Calibrators," *Astronomy and Astrophysics*, vol. 61, pp. 99–106, 1977.

[3] M. J. Klein and C. T. Stelzried, "Calibration Radio Sources for Radio Astronomy: Precision Flux Density Measurements at 2295 MHz," *the Astronomical Journal*, vol. 81, no. 12, pp. 1078–1083, 1976.

[4] P. H. Richter and S. D. Slobin, "DSN 70-Meter Antenna X- and S-Band Calibration Part I: Gain Measurements," *The Telecommunications and Data Acquisition Progress Report 42-97, January–March 1997*, pp. 315–351, Jet Propulsion Laboratory, Pasadena, California, May 15, 1989. http://ipnpr.jpl.nasa.gov/progress_report/

[5] A. J. Freiley, P. D. Batelaan, and D. A. Bathker, *Absolute Flux Density Calibrations of Radio Sources at 2.3 GHz*, JPL Technical Memorandum 33-806, Jet Propulsion Laboratory, Pasadena, California, December 1, 1977.

[6] J. D. Kraus, *Radio Astronomy*, McGraw-Hill, New York, New York, pp. 97–101, 1966.

[7] P. Richter, *Radio Source List for Antenna Calibration*, JPL D-3801, DSN No. 890-269 (internal document), Jet Propulsion Laboratory, Pasadena, California, October 15, 1994.

[8] B. L. Ulich and R. W. Haas, "Absolute Calibration of Millimeter-Wavelength Spectral Lines," *Astrophysical Journal Supplement Series*, vol. 30, pp. 247–258, 1976.

[9] M. Adler, *Cassini Project Policies and Documents*, JPL D-9945, Rev. D (internal document), Jet Propulsion Laboratory, Pasadena, California, 1995.

[10] P. Richter, "Estimating Errors in Least-Squares Fitting," *The Telecommunications and Data Acquisition Progress Report 42-122, April–June 1995*, Jet Propulsion Laboratory, Pasadena, California, pp. 107–137, August 15, 1995. http://ipnpr.jpl.nasa.gov/progress_report/

[11] R. N. Treuhaft and G. E. Lanyi, "The Effect of the Dynamic Wet Troposphere on Radio Interferometric Measurements," *Radio Science*, vol. 22, no.2, pp. 251–265, 1987.

[12] D. Rochblatt, P. Richter, and P. Withington, "On-the-Fly Mapping for Calibrating Directional Antennas," *NASA Tech Briefs* (NPO-30648), vol. 28, no. 8, pp. 53–55, August 2004.

[13] P. W. Gorham and D. J. Rochblatt, "Effect of Antenna-Pointing Errors on Phase Stability and Interferometric Delay," *The Telecommunications and Data Acquisition Progress Report 42-132, October–December 1981*, Jet Propulsion Laboratory, Pasadena, California, pp. 1–19, February 15, 1998. http://ipnpr.jpl.nasa.gov/progress_report/

[14] D. Rochblatt and P. Withington, "Precision Blind Pointing Calibration of the NASA-JPL-DSN Large Reflector Antennas at Ka-Band (32-GHz)," *EuCAP 2006 – European Conference on Antennas & Propagation*, Session 4A10A – Antenna Measurements (12j), November 9, 2006.

[15] *1st DSN Antenna Calibration Workshop*, JPL D-29992 (internal document), Jet Propulsion Laboratory, Pasadena, California, July 6–9, 2004.

[16] S. J. Bolton, M. Janssen, R. Thorne, S. Levin, M. Klein, S. Gulkis, T. Bastian, R. Sault, C. Elachi, M. Hofstadter, A. Bunker, G. Dulik, E. Gudim, G. Hamilton, W. T. K. Johnson, Y. Leblanc, O. Liepack, R. McLeod, J. Roller, L. Roth, and R. West, "Ultra-Relativistic Electrons in Jupiter's Radiation Belts," *Nature*, vol. 415, pp. 987–991 February 28, 2002.

[17] D. J. Rochblatt and B. L. Seidel, "Performance Improvement of DSS-13 34-Meter Beam-Waveguide Antenna Using the JPL Microwave Holography Methodology," *The Telecommunications and Data Acquisition Progress Report 42-108, October–December 1991*, Jet Propulsion Laboratory, Pasadena, California, pp. 253–270, February 15, 1992. http://ipnpr.jpl.nasa.gov/progress_report/

[18] M. J. Klein, S. J. Bolton, A. J. Freiley, S. Gulkis, M. A. Janssen, S. J. Levin, D. J. Rochblatt, J. P. Roller, and R. K. McLeod, "DSN and GAVRT Observations of Jupiter at 13 GHz and the Calibration of the Cassini Radar Instrument for Passive Radiometry," *URSI General Assembly*, Naastrichthe, Netherlands; August 17–24, 2002.

[19] C. Stelzried, "Noise Adding Radiometer Performance Analysis," *The Telecommunications and Data Acquisition Progress Report 42-59, July and August 1980*, Jet Propulsion Laboratory, Pasadena, California, pp. 98–106, October 15, 1980. http://ipnpr.jpl.nasa.gov/progress_report/

[20] C. Stelzried, "Correction of High-Frequency Noise-Temperature Inaccuracies," *The Telecommunications and Data Acquisition Progress Report 42-111, July–September 1992*, Jet Propulsion Laboratory, Pasadena, California, pp. 269–277, November 15, 1992. http://ipnpr.jpl.nasa.gov/progress_report/

[21] C. T. Stelzried, "Noise Temperature and Noise Figure Concepts: DC to Light," *The Telecommunications and Data Acquisition Progress Report 42-67, November and December 1981*, Jet Propulsion Laboratory, Pasadena, California, pp. 100–111, February 15, 1982. http://ipnpr.jpl.nasa.gov/progress_report/

[22] R. Levy, *Structural Engineering of Microwave Antennas*, IEEE Press: Hackensack, New Jersey, 1996.

[23] P. Stumpff, translation of "Astronomische Pointing Theorid Fuer Radioteleskope," *Klein Heubacher Berichte*, vol. 15, Fornmolde Technischon Zentralamt, Darmstadt, Germany, pp. 432–437, 1972.

[24] D. J. Rochblatt, "Holographic Measurements of the NASA-JPL Deep Space Network Antennas," *Proceedings of the 1998 IEEE Aerospace Conference*, Vol. 3, Snowmass at Aspen, Colorado, pp. 441–452, March 21–28, 1988.

[25] D. Rochblatt, P. Richter, P. Withington, M. Vasquez, and J. Calvo, "New Antenna Calibration Techniques in the Deep Space Network," *The Interplanetary Network Progress Report* vol. 42-169, pp. 1–34, May 15, 2007. http://ipnpr.jpl.nasa.gov/progress_report/